Reducing Emitter Localization Error in Urban Environments with Geometry Adaptive UAS Arrays

Christopher Peters
Electrical & Computer Engineering
Southern Methodist University
Dallas, TX
peterscl@smu.edu

Mitchell A. Thornton
Darwin Deason Institute for Cyber Security
Southern Methodist University
Dallas, TX
mitch@smu.edu

***Abstract*— A geometrically-adaptable cooperative unmanned aerial system (UAS) array provides enhanced localization accuracy in radio frequency (RF) emitter localization over that of a stationary array. We investigate such an array in simulated urban settings, where atmospheric scattering and building multipath impacts localization accuracy. The research leverages the time difference of arrival (TDOA)-based Location on a Conic Axis (LOCA) algorithm to estimate emitter locations, demonstrating improved accuracy through iterative updates to the geometry of the UAS sensor array. The research analyzes dynamic repositioning approaches for the UAS array, showing how an array that adapts to changing environmental conditions with new sensor geometries will reduce localization error over successive searches. Further, we show that using environmental feedback and exploiting the LOCA geometry to adapt the UAS geometry at a large distance facilitates remote localization as an improvement over traditional received signal strength (RSS) based methods that require physical convergence of the UAS to the emitter. Our results demonstrate that optimal UAS placement and dynamic repositioning are viable opportunities to improve localization performance in dense urban settings.**

***Keywords*— Cooperative UAS, TDOA, multipath propagation, localization, adaptive geometry arrays**

I. Introduction

Unmanned aerial systems (UAS) equipped with passive RF sensors, such as represented in Fig. 1, are increasingly being deployed in complex environments for emitter localization. These UAS networks leverage wireless ad hoc connectivity to form cooperative arrays that can adapt their sensor geometries and optimize mission performance. For instance, in a search and rescue operation in a challenging environment, such as a dense urban area, the UAS array can reconfigure its geometry to improve the geolocation estimate of an unknown-location emergency beacon. Further, in hostile environments where the UAS array cannot physically converge on the emitter, such as tactical regions or due to fire or other harsh conditions, an accurate localization capability is required from a remote or "standoff" distance. In these settings, subgroups of elements of the UAS array can cooperatively and independently localize the emitter, such that the localization accuracy depends on both the accuracy of the full cooperative UAS array and/or the independent UAS subarrays, thus increasing the effectiveness of a large array of UAS by exploiting the subarray operation.

In this work, we evaluate the impact of challenging environments, such as dense urban settings that are subject to multipath and atmospheric impacts, to emitter localization with cooperative UAS systems and consider the analysis of local hardware errors from [1] to evaluate an accumulated localization error. To assess the environmental impacts, this study utilizes stochastic models of urban propagation loss from International Telecommunication Union (ITU) Recommendation P.1411-12 [2] and demonstrates that the mobility of a cooperative UAS network improves emitter localization accuracy through dynamic repositioning.

The UAS repositioning approach extends beyond traditional localization approaches such as that performed by fixed-wing aircraft, and it can only be performed by a highly mobile UAS network. The availability of a practical repositioning method could potentially reduce UAS mission planning while enabling operations in more complex environments. Our repositioning scheme is informed by both UAS array and subarray emitter localization estimates, using a time difference of arrival (TDOA) algorithm, combined with measurements of emitter received signal strength (RSS). The approach herein differentiates itself from other UAS localization approaches that reposition based on emitter RSS or focus on optimizing sensor geometry [3]-[7], because these other methods do not utilize real-time feedback from environmental conditions. Furthermore, RSS-based optimization methods assume conditions that allow physical convergence to an emitter. We present a method that does not require such convergence and its ability to overcome environmentally-sourced errors while physically remote.

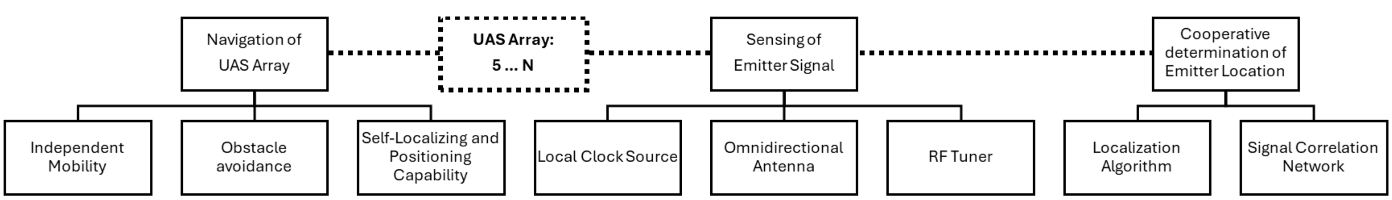

Fig. 1. UAS Emitter Localization System Representative Functional Block Diagram.

The contributions of this work include a detailed analysis of environmental error contributions in complex urban scenarios for cooperative UAS array emitter localization, considerations of practical limitations with hardware and environmental constraints, and a geometrically adaptable UAS system that improves localization performance even at standoff distances.

II. Related Work

The authors in [1] examined UAS sensor hardware errors on emitter localization accuracy, focusing on cooperative UAS sensor positioning and time-of-arrival (TOA) errors, while assuming environmental effects like atmospheric refraction and multipath scattering to be negligible. However, quantifying environmental impacts is needed in complex environments like dense urban areas where building interiors and tree canopies create multipath effects that significantly impact localization accuracy. In these scenarios, assuming constant signal propagation velocity overlooks the impact of atmospheric refraction and multipath due to metallic and other reflective structures. While incorporating dynamic signal propagation models could mitigate these effects, this study assumes these resources are not available and integrates multipath impacts directly into the localization process. Thus, we provide an extensive error analysis and model for these scenarios to evaluate operational suitability.

In consideration of UAS repositioning methods, in [3],[4], the authors optimize the geometric configuration of the UAS to improve the accuracy of the localization based on the RSS. We implement the notion of this RSS-based approach and extend it by quantifying the capability with a robust environmental error model. However, these RSS methods and related ones either rely on pre-defined optimized geometries that do not consider the dynamics of a complex RF signal environment [4], [5], they are computationally complex utilizing low-rank optimization and trajectory planning [5], [6], or they consider only RSS [3]-[5], which may not be useful in geography-constrained situations.

The authors of [5] utilize RSS and add a complex algorithm to perform collaborative processing within the UAS to improve the inter-UAS positioning estimates. They combine these measurements with angle of arrival data and implement super multidimensional scaling with patch dividing/merging techniques. In a similar level of complexity, the authors of [6] perform a dynamic repositioning approach utilizing semidefinite programming and alternating convex optimization to determine the emitter location and the UAS iterative geometry via pre-determined waypoints. Further, approaches such as [6] and [7] consider trajectory planning with a single UAS and do not consider a cooperative UAS array.

While effective, many of these methods are computationally demanding and require physical convergence on the emitter. Our study examines similar approaches, yet we differentiate our work by showing that utilizing a localization algorithm while remaining at a distant range and incorporating real-time environmental feedback to inform iterative updates to the sensor geometry provides a continuous refinement of localization estimates. We utilize a low-complexity and computationally efficient localization algorithm and offer a practical, real-time approach, based on geometry and timing, with omnidirectional antennas, allowing for distributed processing at the individual UAS, so that the system is adaptable in complex environments with scaling UAS array sizes.

III. Path Loss Models

In a sensing scenario where the RF transmitting power of the emitter is unknown, a given sensor s_i of $i = 1 \ldots N$ sized array will receive a power level that is the radiated power of the emitter, P_e, reduced by the loss in that sensor L_{si} and environmental path loss from the emitter to the sensor. With an omnidirectional antenna, this is the RSS of s_i, RSS_i, and can be expressed as (1):

$$RSS_i = P_e - L_{si} - \sum L_{PLi}, \tag{1}$$

where $\sum L_{PLi}$ is the total environmental path loss from the emitter to the sensor. For the purposes of this effort, we assume that L_{si} is known and therefore will be neglected.

Determining $\sum L_{PLi}$ requires an understanding of the scattering mechanisms present in the propagation environment, including free space path loss L_{fsi}, contributions from the moisture in the atmosphere L_{atm}, and local scatterers L_{ref} such as the landscape, roads, buildings, and other structures. The path loss is defined by the total contribution of each of these sources:

$$\Sigma L_{PLi}(dB) = L_{fsi} + L_{ref} + L_{atm}. \tag{2}$$

In a scattering-free environment, L_{fsi} is:

$$L_{fsi}(dB) = 20\log_{10}\left(\frac{4\pi R_i f}{c}\right), \tag{3}$$

where R_i is the distance from the emitter to sensor s_i, f is the transmitting frequency of the RF signal, and c is the speed of light. For a given L_{PLi} the estimated distance $\hat{R}_i$ between a sensor and emitter pair could be found by transforming the free space equation into terms of R_i, and the signal transmit time across the path can be found by dividing $\hat{R}_i$ by c

$$\hat{t}_i = \frac{\hat{R}_i}{c} = \frac{\lambda}{4\pi c} 10^{\sum L_{PLi}/20}. \tag{4}$$

In the presence of scatterers, $\sum L_{PLi}$ will be greater than L_{fsi}, leading to inaccuracies in $\hat{R}_i$.

A. Urban Environment Path Loss

In [8], path loss profiles are surveyed for a variety of UAS-to-emitter scenarios. In this text it was discussed that a best fit for an urban environment with a number of scatterers is a dual-slope path loss model that changes as R_i increases. The ITU-R P.1411-12 [2] formulates a stochastic dual-slope path loss model incorporating height-dependent scenarios in urban environments. In Section 4 of [2], the effects of streets and buildings are examined with a single-bounce geometry to provide expected path loss in both line-of-sight (LoS) and non-line-of-sight (NLoS) conditions between the transmitter and receiver. The model considers transmitters and receivers operating below- and above-building rooftops, assuming that building heights follow a Rayleigh distribution. Further, the model parameters of average building height, average street and building widths, and average number of buildings in given land area, can be modified for the type of physical operating environment: urban high-rise, urban low-rise, suburban, and residential. Finally, for each scenario, both a generalized statistical model and a site-specific model are provided for 3-dimensional urban profiles.

The median loss for a given urban scenario is found by [2]:

$$L_b(dB) = 10\alpha \log_{10}(R_i) + \beta + 10\gamma \log_{10}(f) + L_\sigma \quad (5)$$

where α is a coefficient associated with the increase of basic transmission loss with distance, β is a coefficient associated with the offset value of the basic transmission loss, γ is a coefficient associated with the increase of the basic transmission loss with frequency, and L_σ is a zero mean Gaussian random variable, $\mathcal{N}(0, \sigma^2)$, with standard deviation, $\sigma(dB)$, defined for specific scenarios. For NLoS urban environments, the model states that there will be an excess loss with respect to free space that will not exceed:

$$NLoS_{excess}\ (dB) = (10^{0.1A} + 1), \quad (6)$$

where A is a Gaussian random variable, $N(\mu, \sigma^2)$, with σ defined above and mean given by:

$$\mu(dB) = L_b - L_{fsi}. \quad (7)$$

In [2], Tables 4 and 8 provide the values of the above coefficients ($\alpha, \beta, \gamma, \mu, \sigma$) that are relevant to the simulations herein. For the propagation height, “Below Rooftop” is a scenario where both the transmitter and receiver are below the height of the roofs of the buildings in the range, whereas “Above Rooftop” refers to the scenario where either of the transmitter or receiver are located above the rooftop. In the “Above Rooftop” case, it is assumed the link can be described with L_{fsi}. Because the model statistically formulates loss profiles, shadowing effects of buildings are incorporated into coefficients such as L_σ, so the associated loss increases more than free space loss with increasing R_i. The model claims validity for frequencies of 300 MHz to 100 GHz and the coefficients in [2] are valid for the ranges specified.

For this analysis, MATLAB is used to model the signal interactions, however, because MATLAB does not offer a direct implementation of ITU-R P.1411, the models were custom-programmed. To ensure that the model would be effective over the full ranges in this study, the coefficient values were extrapolated to distances approximately 15% outside the model specified ranges.

B. Multipath Fading

The reflections of a signal against local scatterers will cause multipath fading depending on the geometry and characteristics of the environment. Two fading models, Rician and Rayleigh, are widely used to statistically model fading for LoS and NLoS conditions, respectively. Multipath fading is modeled according to the path loss profile of the propagation channel, the path delay between the primary and multipath component, and the Rician K-factor which is the ratio of the dominant channel component to the sum of all other components. A Rician distribution is usually appropriate to model the small-scale amplitude fading formed from an airborne UAS system to a stationary ground-based emitter [8].

The multipath K-factor is scenario-dependent, and values of 28 dB have been found to be appropriate for a UAS mission in an urban area [9], [10]. For this analysis, the MATLAB Communications Toolbox [11] was utilized to generate the multipath fading characteristics, using the empirical path delay spread and path loss models from [2]. For the “Below Rooftop” scenario described previously, the impact of scatterers in different geometries and environments is accounted for using Gaussian random variables with mean and standard deviation determined by coefficients defined in Table 12 of [2] for different scenarios of the model. Similarly, for the “Above Rooftop” scenario, the median “RMS Delay Spread” is determined with scenario-specific coefficients found in Table 10 of [2].

Fig. 2 represents the delay spread profiles from [2] over a fixed distance and compares the mean delay spreads for the above and below rooftop conditions from the signal delay value determined by (4). The mean delay spread for the below rooftops condition not only exceeds the delay spread for the above rooftops condition due to building and ground scattering, but this difference spread could vary significantly. As the distance from the emitter to the sensor is increased to 1 km, the path loss is found both by L_{fsi} and L_b determined by [2]. By using (4) alone, the median signal strength in an urban environment could cause ambiguities in sensor-emitter range determination. Therefore, the use of the time delay from the signal to sensors in various positions could resolve this uncertainty and potentially inform characteristics of the scattering environment.

C. Atmospheric Path Loss

As a signal travels through the atmosphere, it is attenuated according to the geometry and density of moisture, such as rain or water vapor (fog), in its path. The ITU Recommendation P.838-3 [12] offers an empirically-derived signal attenuation model for determining the impact of rainfall on signal attenuation using a statistical rain rate to determine the signal loss at a specific frequency over a specified range. Further, the ITU Recommendation P.676-10 [13] considers ambient temperature, pressure, and atmospheric water vapor density to determine the signal loss at a specific frequency over a specified

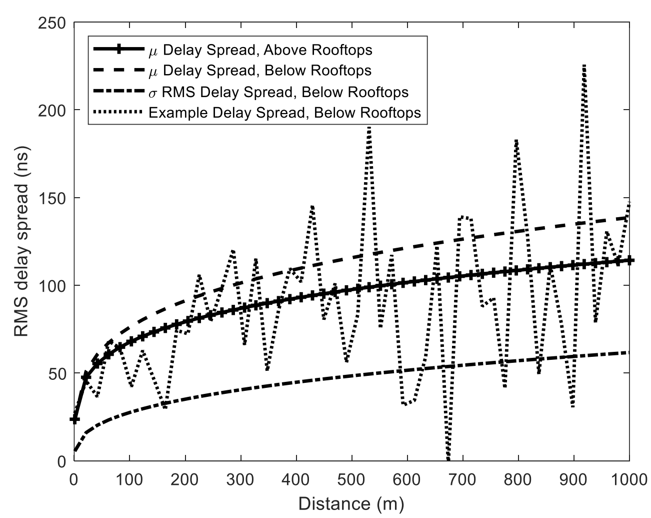

Fig. 2. Comparison of delay spread profiles in height-specific geometries.

range. The MATLAB Communications Toolbox [11] provides, among other capabilities, implementations of the above water vapor model and the rain model, extended with the work in [14], for atmospheric path loss, and those models are used in the simulations in this study.

Other atmospheric models were not utilized because they fell outside the parameters of this study. For example, ionospheric and tropospheric models consider a signal propagating at an altitude much greater than the 500m height that is considered in this analysis. Models for fog are generally valid for frequencies greater than 10 GHz, while this analysis considers a 5 GHz signal with the assumption that the UAS array is likely to be processing 5G New Radio (NR) signals [15]. Modeling a "severe" moisture condition for a 5 GHz signal, rain dominates the environmental impact; however, the accumulated atmospheric loss is only approximately 0.5dB at 1km.

IV. Localization and Repositioning Algorithms

A. Localization Algorithm and Collective Estimate Radius

The study in [1] considered timing-based localization algorithms, i.e. multilateration and Location on a Conic Axis (LOCA), that did not require phase coherent receivers for each UAS. The LOCA algorithm, originally formulated by Schmidt [16] [17], employs the TDOA of signals across a triad of sensors to determine the emitter's location. The algorithm determines an emitter location by calculating a straight line through an axis of a conic section, where the sensors are positioned along the perimeter of this conic and the emitter at its focus. An example of this geometry in two-dimensions is shown in Fig. 3.

LOCA considers the difference in estimated range to the target for a triad of sensors i, j, k:

$$\Sigma = \Delta R_{ij} + \Delta R_{jk} + \Delta R_{ki}. \quad (8)$$

where ΔR_{mn} represents the difference in range to the target from sensors m and n. Using a_i to represent the absolute range of sensor i to the origin of the coordinate system,

$$a_i = \sqrt{{x_i}^2 + {y_i}^2 + {z_i}^2}, \quad (9)$$

the algorithm implements these range differences in a set of linear equations to find the conic axis:

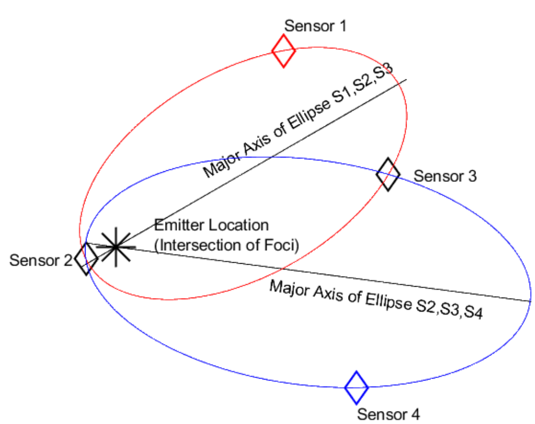

Fig. 3. Intersection of two conic major axes at emitter location found by LOCA algorithm.

$$\begin{gathered}[x_1\Delta R_{23} + x_2\Delta R_{31} + x_3(\Delta R_{12} - \Sigma)]x + \\ [y_1\Delta R_{23} + y_2\Delta R_{31} + y_3(\Delta R_{12} - \Sigma)]y + \\ [z_1\Delta R_{23} + z_2\Delta R_{31} + z_3(\Delta R_{12} - \Sigma)]z = \\ \tfrac{1}{2}[\Delta R_{12}\Delta R_{23}\Delta R_{31} + {a_1}^2\Delta R_{23} + {a_2}^2\Delta R_{31} + {a_3}^2(\Delta R_{12} - \Sigma)]\end{gathered}. \quad (10)$$

For three dimensions, (10) is in the form of the plane equation and is solvable with linear algebra techniques. For ambiguity resolution among the conic focal points, LOCA has a lower bound minimum requirement of five UAS sensors, resulting in three conic planes intersecting at a common location, the conic focus, which is the emitter location [17]. With a set of $N \geq 5$ sensors, there are $\binom{N}{3}$ sensor i, j, k triads that can be formed, and any combination of a subset of 5-to-N of these triads can produce the emitter location estimate. The maximum number of intersections can be determined combinatorially by (11), and for a system of 8 cooperative sensors, this results in 130 location estimates determined for a correlated signal:

$$\mathrm{intersects}_{\mathrm{max}} = \sum_{\mathrm{k}=5}^{\mathrm{N}} \sum_{\mathrm{i}=\mathrm{k}}^{\mathrm{N}} \binom{\mathrm{i}}{\mathrm{k}}. \quad (11)$$

Fig. 4 presents an example of how the number of emitter location estimates increases with increasing sensor quantities and shows the density of the collection of estimates. The system utilizing this algorithm in the presence of environmental errors could determine the most probable emitter location and utilize the density of estimates to refine its solution. For this, we consider the radius of the 50% spherical error probable (SEP) [22] determined by averaging the results obtained by the LOCA algorithm for every available sensor combination. The SEP of the location estimate is based on the mean of the emitter location estimates, also known as the centroid. This radius extends from the centroid and is determined by the median absolute deviation from the centroid to the individual estimates.

B. Error Accumulation

In addition to analyzing the impact of environmental scatterers, we include hardware error models from [1] to evaluate a cumulative error for the cooperative UAS. For TDOA localization algorithms, it is necessary to know the error contribution from UAS sensor position estimates and clock synchronization offsets that could cause TDOA errors when correlating a time-stamped signal. It is assumed for this study that the system is capable of adequately correlating received signals since previous work [18]-[21] has resulted in acceptable

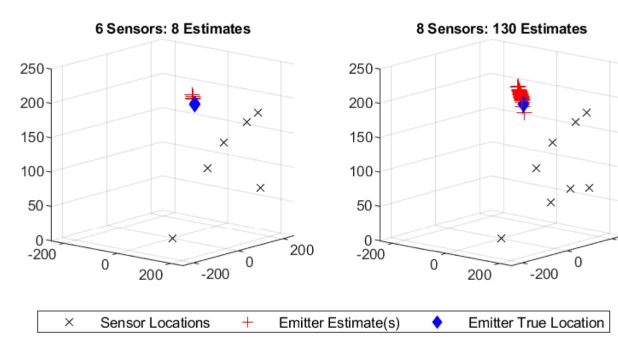

Fig. 4. Density of LOCA estimates with increasing sensor quantities.

methods for correlating continuous signals at spatially separated sensors and correlating pulse signals via rising or falling edges.

The timing error augments the range estimate (8) by (12):

$$\hat{R} = c\left(t_c + t_a + t_m - 2t_f\right), \tag{12}$$

where t_c is the signal TOA in the presence of sensor timing inaccuracy from [1], t_a and t_m are the signal TOAs in the presence of atmospheric scatterers and multipath, respectively, and $2t_f$ is a free-space TOA correction for the environmental error offsets (since it is accounted for in t_c). Further, the positioning error augments the sensor positions in (9) and (10) by (13), where $(\varepsilon_{xi}, \varepsilon_{yi}, \varepsilon_{zi})$ correspond to the sensor positioning error:

$$\hat{x}_i = x_i + \varepsilon_{xi}, \quad \hat{y}_i = y_i + \varepsilon_{yi}, \quad \hat{z}_i = z_i + \varepsilon_{zi}. \tag{13}$$

In the study of error contributions from the UAS positioning and timing hardware [1], the Cramér-Rao lower bound (CRLB) for TDOA measurements was derived to assess the theoretically achievable accuracy for a TDOA system such as this. The CRLB of the variance σ_i^2 is the inverse of the Fisher Information Matrix (FIM) $\boldsymbol{J}$, expressed in terms of the TDOA τ. For positioning errors, this leads to the FIM in (14):

$$\boldsymbol{J}_\tau = \begin{bmatrix} \frac{\partial\tau_2}{\partial x} & \frac{\partial\tau_3}{\partial x} & \cdots & \frac{\partial\tau_n}{\partial x} \\ \frac{\partial\tau_2}{\partial y} & \frac{\partial\tau_3}{\partial y} & \cdots & \frac{\partial\tau_n}{\partial y} \\ \frac{\partial\tau_2}{\partial z} & \frac{\partial\tau_3}{\partial z} & \cdots & \frac{\partial\tau_n}{\partial z} \end{bmatrix} \boldsymbol{R}_{TDOA}^{-1} \begin{bmatrix} \frac{\partial\tau_2}{\partial x} & \frac{\partial\tau_2}{\partial y} & \frac{\partial\tau_2}{\partial z} \\ \frac{\partial\tau_3}{\partial x} & \frac{\partial\tau_3}{\partial y} & \frac{\partial\tau_3}{\partial z} \\ \vdots & \vdots & \vdots \\ \frac{\partial\tau_n}{\partial x} & \frac{\partial\tau_n}{\partial y} & \frac{\partial\tau_n}{\partial z} \end{bmatrix}^T \tag{14}$$

where $\boldsymbol{R}_{TDOA}$ is the covariance matrix of sensor positioning errors σ_i^2.

For the timing error, we consider the signal propagation speed c, receiver bandwidth B, the optimal signal-to-noise ratio SNR_0, the range to the emitter r_i, and the ideal lower threshold for the system operating range, r_0:

$$\sigma_i{}^2(r) \geq \frac{c^2}{B^2 SNR_0}\frac{r_i{}^2}{r_0{}^2}. \tag{15}$$

The FIM in (14) takes the form of

$$\boldsymbol{J}_\tau = \left(\frac{\partial\tau(x)}{\partial x_i}\right)^T \boldsymbol{R}(\boldsymbol{x})^{-1}\frac{\partial\tau(x)}{\partial x_j} + \frac{1}{2} tr\left(\boldsymbol{R}(\boldsymbol{x})^{-1}\left(\frac{\partial\sigma_{i1}}{\partial x_i}\right)^T \boldsymbol{R}(\boldsymbol{x})^{-1}\frac{\partial\sigma_{i1}}{\partial x_j}\right), \tag{16}$$

with a parameter-dependent FIM Jacobian of

$$\frac{\partial\sigma_{i1}}{\partial\boldsymbol{x}} = \frac{\sqrt{a}(r_i+r_1)}{r_0\sqrt{SNR_0(r_i{}^2+r_1{}^2)}}. \tag{17}$$

With the hardware and environmental error contributions formulated and with the theoretical lower bound assessed, we use this information to quantify the impact of these errors in emitter localization accuracy.

C. Repositioning Methodology

In the presence of the defined errors, we consider an approach to improve the localization accuracy using dynamic repositioning of the UAS array. To address blocked LoS and other challenges in urban environments, our methodology involves strategic repositioning of the UAS elements. Real-time assessments using RSS and TDOA data guide the dynamic adjustments within the framework of the LOCA algorithm. The system benefits from the computational efficiency of LOCA and operational flexibility of the UAS array, enabling it to maintain optimal sensor configurations in response to evolving environmental conditions.

Once the emitter location estimate is determined, a repositioning scheme is applied to the sensor locations, where a sensor subarray corresponding to a certain suboptimal condition is relocated to a new position and the target position is subsequently estimated. The approach continues with the new sensor locations to iteratively reposition the array. By only repositioning the subset of the UAS array that corresponds to the suboptimal conditions, we adapt the geometry to the environment and expect to improve the overall localization accuracy. We consider as a performance metric the improvement of the SEP radius for each iterative repositioning. Two methods are based on geometrically converging a subarray on the centroid to reduce the range-based error, while one method is based on randomly repositioning a subarray to potentially remove a NLoS condition. The last method finds an equal range to the centroid for a subarray to reduce the TDOA errors, the goal of which is to exploit the inherent geometry of the LOCA algorithm to find optimal positions without geometrically converging on the emitter. These repositioning schemes are as described below for each localization step:

{I} RSS Convergence:

1. Determine the emitter estimate centroid and the range from each sensor to the centroid, R_i, using (10).
2. Identify the three sensors, s_i, s_j, s_k, with the lowest RSS, such that $RSS_i \leq RSS_j \leq RSS_k \leq \cdots \leq RSS_n$.
3. Reposition s_i, s_j, s_k to a location 25% closer to the centroid.

{II} Best Estimate Random:

1. Determine the emitter estimate centroid and the range from each sensor to the centroid, R_i, using (10).
2. Consider from (10) the contribution of each s_i to the set of emitter estimates (130 estimates for the 8 UAS system).
3. Next, determine the median absolute deviation from the centroid for each estimate and associate that deviation with each sensor used for that estimate.
4. Compute the total deviation for each sensor as a sum of all deviations associated with that sensor.
5. Identify s_i, s_j, s_k with the highest deviation.
6. Reposition the subarray s_i, s_j, s_k to a random position.

{III} Best Estimate Convergence:

1. Perform methodology in {II} through step {5}.
2. After identifying s_i, s_j, s_k, reposition the subarray to a location 25% closer to the centroid.

{IV} Best Estimate Equidistant:

1. Perform methodology in {II} through step {5}.
2. After identifying s_i, s_j, s_k, reposition the subarray to a location that is the mean range of s_i, s_j, s_k to the centroid.

V. Simulation Approach and Results

A. Simulation Approach

For this analysis, the emitter-sensor system was modeled in MATLAB, where the emitter was assumed stationary and broadcasting a 5 GHz signal with known signal characteristics and sufficient SNR in the far-field of the UAS system. The sensor and emitter initial locations were uniformly randomized, in a simulated urban environment that is approximately 1500m wide, long, and high. The UAS sensor system followed the representation in Fig. 1, with quantities $N \geq 5$, with a LiDAR-based UAS self-positioning system that has an accuracy of 2 cm, and a local clock source with an accuracy of 10 ns. The self-positioning accuracy is supported by products such as Texas Instruments compact LIDAR solution [23] that permits a ranging accuracy of 1cm at 100m, which is better than GPS [24]. Likewise, the low local timing source error is supported by small portable "Chip Scale Atomic Clocks" (CSAC) that provide a basis for high resolution local timing sources with low drift and jitter rates [25], [26] with ≤ 1 ns accuracy. Even without the presence of timing source synchronization methods, the use of a CSAC-based local timing source allows for a low-latency free-running timing source that is synchronized at pre-mission time only, and it is therefore a reasonable approach to enable accurate emitter location estimates over limited mission durations.

The simulations were modeled for both an urban low-rise and an urban high-rise scenario, and the path loss profiles were modeled in MATLAB using the methodology in ITU-R P.1411 [2]. Because the localization algorithm is time-based, the TOA of the signal to each sensor was determined with (4) by using the estimated path loss. For atmospheric scatterers, the Crane [14] model assumed a maximum rain rate of 30 mm/hr and a maximum water vapor of 30 $\mathrm{g/m^3}$, each of which can be considered "worst-case" weather conditions.

We use Monte Carlo simulations with 1000 runs to characterize the impact of these errors on the performance of the algorithm. The emitter location estimate was determined using the LOCA algorithm for each Monte Carlo result. The UAS positions and the emitter were then randomly varied 500 times to remove bias in the results. A localization error metric was calculated by finding the Euclidean distance from the true emitter location to the emitter location estimate. After each initial localization, the UAS repositioning approaches {I}-{IV} were independently modeled for 25 steps. At each step, the localization estimate was repeated using the described MATLAB simulation environment to inform the accuracy improvement in dynamic repositioning.

B. Simulation Results

In each urban setting, we examined the initial localization error by averaging the LOCA-derived emitter positions across Monte Carlo simulations, incorporating increasing sensor quantities and randomized initial conditions. The localization error results shown in Fig. 5 indicate that increasing the number of sensors mitigates the influence of environmental and hardware error; however, there is not a significant improvement to accuracy with more than nine sensors. This result is consistent with the results in [1] and shown here for comparison, where a system under the constraints of local clock inaccuracies and

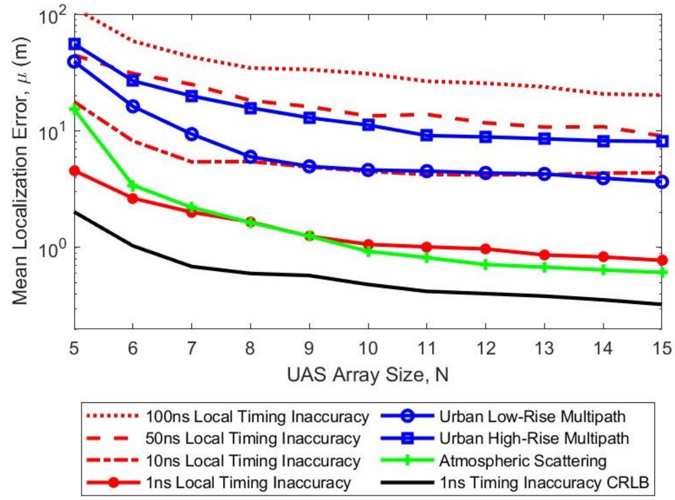

Fig. 5. Localization error due to environmental scatterers with up to 15 sensors compared to errors due to sensor hardware inaccuracies.

sensor positioning errors does not result in a localization accuracy improvement with more than nine sensors. Therefore, the remainder of the study considers a maximum of nine sensors.

Evaluating the environmental path loss impacts against the individual error contributions from [1], that is, the timing inaccuracies, positioning error, and the time-based CRLB, the atmospheric scattering alone provides a much lower localization error than urban multipath and is on a similar order as a system with 1 ns local timing inaccuracy. In an urban low-rise environment, the system appears to converge to similar accuracy as a system with 10 ns local timing inaccuracy. An urban high-rise environment will provide lower accuracy than the low-rise scenario, and it provides an error slightly lower than that of a system with 50 ns timing inaccuracy.

In Fig. 6, we accumulate the environmental and hardware errors for both urban multipath settings and present the localization error distribution across Monte Carlo runs for random emitter positions and random initial, i.e. static, sensor positions for different UAS array sizes N. For both urban settings, the mean localization error μ improves with increasing

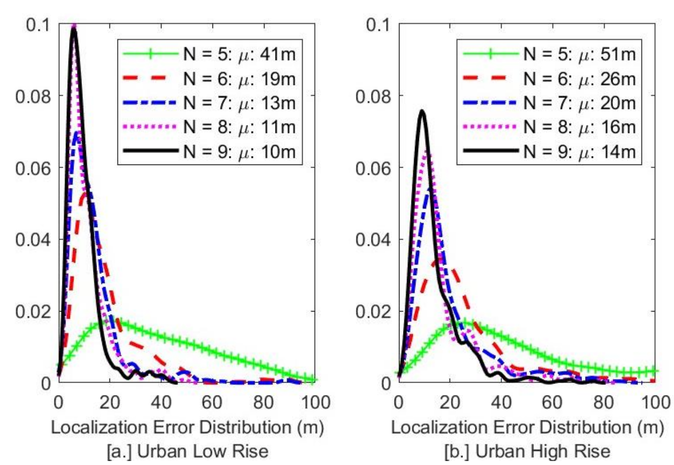

Fig. 6. Distribution of localization error with mean error μ for increasing sensor quantity N in [a.] urban low-rise and [b.] urban high-rise environments with static UAS.

N with the most significant improvement from $N = 5$ to $N = 6$. In an urban setting, and especially in a high-rise environment, the inclusion of a sixth sensor appears to resolve the errors introduced by the scatterers. In addition to the improvement in mean localization accuracy, the distribution shows that the density of results with high accuracy increases with the quantity of sensors, driven by the combinatorial advantages of the LOCA algorithm.

Although the additional sensors provide increasing localization accuracy in the presence of environmental scatterers, we are seeking to maximize this accuracy for all sensor quantities by exploiting the mobility of the UAS network and utilizing the cooperative aspect of the UAS array via emitter localization at the subarray-level. Therefore, we consider the repositioning approaches and the mitigation of the accumulated environmental errors with adaptive UAS geometries. Further, we analyze the SEP radius as a metric to quantify the improvement to the localization accuracy with subsequent geometries, with the assumption that these metrics are correlated. Fig. 7 shows the SEP propagation for the case where no hardware or environmental errors are present. In this case, the RSS and the equidistant approaches continually improve the SEP, while the methods of random repositioning and best estimate convergence maintain a nearly static SEP radius & localization error. For the RSS method, this is expected as all elements eventually migrate towards the target and ensure their TDOA, and thus their solution offset, is minimized. The best estimate convergence approach remains static because, in an error-free case, the localization estimates completely converge regardless of sensor position, while the TDOA will not necessarily converge as in the case of the equidistant approach.

We apply our repositioning methods in a scenario representative of an urban scattering environment with a 10 ns local timing inaccuracy and 2 cm UAS positioning error and with 6- and 9-element UAS arrays. The dynamic repositioning results presented in Fig. 8 show the SEP radius and localization error improvement normalized to the initial SEP radius and localization error for each scenario. In general, as the search algorithm repositions the sensor array, the SEP radius and localization error decreases, except for the random repositioning approach, which shows no improvement. The RSS method offers the greatest improvement, which is a direct result of the path loss models from [2], such that a smaller propagation

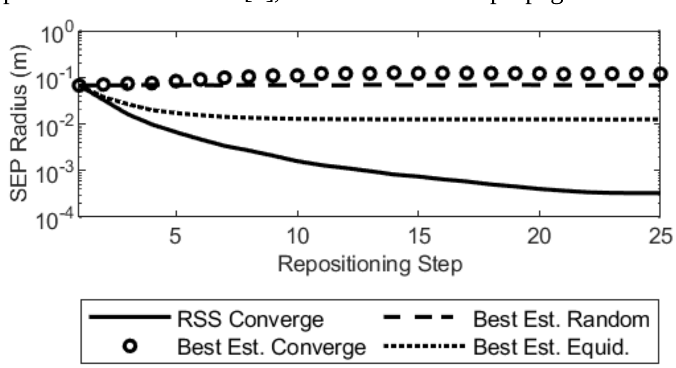

Fig. 7. Spherical error probable (SEP) radius with iterative geometries in error-free environment by repositioning subarray with: 1) lowest RSS towards centroid, 2) largest LOCA deviation to random location, 3) largest LOCA deviation towards centroid, and 4) largest LOCA deviation to equidistant range.

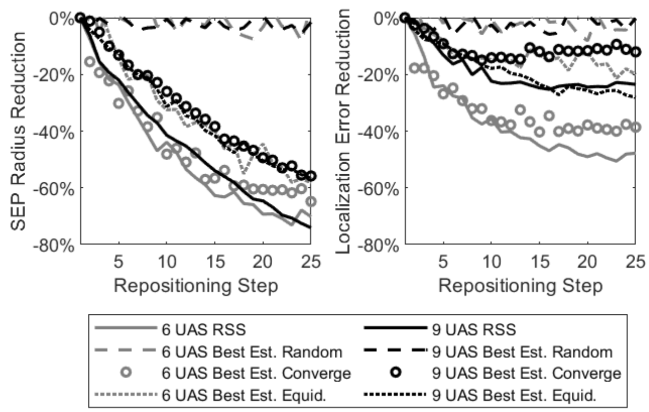

Fig. 8. Reduction in spherical error probable (SEP) radius reduction and localization error as a percentage of initial SEP and localization error for 6-sensor and 9-sensor UAS arrays, in presence of environmental and hardware errors by repositioning subarray with: 1) lowest RSS towards centroid, 2) largest LOCA deviation to random location, 3) largest LOCA deviation towards centroid, and 4) largest LOCA deviation to equidistant range.

distance results in a lower error term compared to the overall signal strength. However, the equidistant approach, which does not rely on physical convergence like RSS, provides a similar reduction in SEP radius and localization error. Further, while the 6-element UAS array offers an overall higher initial localization error than larger arrays as seen in Fig. 6, it experiences a consistently greater improvement to the SEP radius with an adaptive geometry compared to the 9-element UAS case.

The adaptive geometry approach enables the system to minimize environmental and hardware error in its localization performance irrespective of the array size, with a greater impact of improvement with smaller arrays. Further, the equidistant approach provides an alternative to methods that converge on the emitter location, allowing missions to improve their localization accuracy at standoff distances.

Last, we consider mission effectiveness by evaluating localization error as related to the total distance traveled by the UAS for each method. In Fig. 9, we see that for the equidistant method, the UAS travels approximately half the distance of the RSS method to achieve an equivalent localization performance, resulting in a reduced usage of system resources and mission time. The best estimate convergence method has a plateau of performance after traveling the same length as the equidistant method; however, it does not improve its localization accuracy to the same magnitude as the other approaches.

VI. Conclusion

This investigation informs the viability of a reconfigurable cooperative wireless sensor array for emitter localization in an urban environment. Informed repositioning of the UAS sensor array results in improved accuracy in localization without requiring physical convergence on the emitter, proving more mission flexibility than RSS-based methods. The sensor array utilizes the LOCA algorithm to generate target location estimates with its distributed subarrays and with the full array, enhancing its flexibility as a cooperative emitter localization system. The localization error can be minimized with a small quantity of sensors and a low-complexity localization and

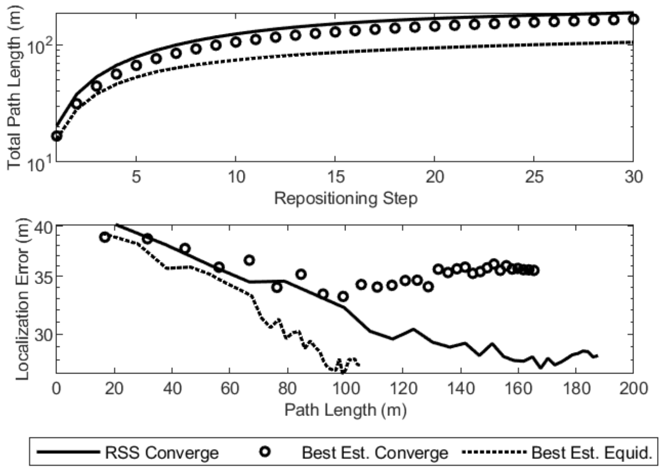

Fig. 9. Comparison of total path length traveled by each UAS and the associated localization error reduction for repositioning subarray with: 1) lowest RSS towards centroid, 2) largest LOCA deviation towards centroid, and 3) largest LOCA deviation to equidistant range.

optimization algorithm, reducing the overall system cost without sacrificing performance. While a 5-sensor cooperative UAS array is minimally suitable for emitter localization with this method, increasing the array size with up to nine sensors significantly enhances accuracy and enables more dynamic missions at both the array- and subarray-level.

In future studies, we explore the use of machine learning methods to optimize UAS sensor positions, driven by the findings that dynamically reconfiguring the array allows for improved emitter localization accuracy.

References

[1] C. Peters and M. A. Thornton, "Cooperative UAS Geolocation of Emitters with Multi-Sensor-Bounded Timing and Localization Error," 2023 IEEE Aerospace Conference, Big Sky, MT, USA, 2023, pp. 1-13, doi: 10.1109/AERO55745.2023.10116023.

[2] Radiocommunication Sector of International Telecommunication Union, "Propagation data and prediction methods for the planning of short-range outdoor radiocommunication systems and radio local area networks in the frequency range 300 MHz to 100 GHz", Rec. ITU-R P. 1411–12 ITU Recommendation, Aug. 2023.

[3] S. Wu, "Illegal radio station localization with UAV-based Q-learning," in China Communications, vol. 15, no. 12, pp. 122-131, Dec. 2018, doi: 10.12676/j.cc.2018.12.010.

[4] X. Cheng, F. Shu, Y. Li, Z. Zhuang, D. Wu and J. Wang, "Optimal Measurement of Drone Swarm in RSS-Based Passive Localization With Region Constraints," in IEEE Open Journal of Vehicular Technology, vol. 4, pp. 1-11, 2023, doi: 10.1109/OJVT.2022.3213866.

[5] R. Chen, B. Yang and W. Zhang, "Distributed and Collaborative Localization for Swarming UAVs," in *IEEE Internet of Things Journal*, vol. 8, no. 6, pp. 5062-5074, 15 March15, 2021, doi: 10.1109/JIOT.2020.3037192.

[6] L. Xiang, M. Zhang and A. Klein, "Robust Dynamic Trajectory Optimization for UAV-aided Localization of Ground Target," *GLOBECOM 2023 - 2023 IEEE Global Communications Conference*, Kuala Lumpur, Malaysia, 2023, pp. 7484-7489, doi: 10.1109/GLOBECOM54140.2023.10437337.

[7] D. Ebrahimi, S. Sharafeddine, P.-H. Ho, and C. Assi, "Autonomous UAV trajectory for localizing ground objects: A reinforcement learning approach," IEEE Trans. Mobile Comput, vol. 20, no. 4, pp. 1312–1324, Apr. 2021.

[8] W. Khawaja, I. Guvenc, D. W. Matolak, U. -C. Fiebig and N. Schneckenburger, "A Survey of Air-to-Ground Propagation Channel Modeling for Unmanned Aerial Vehicles," in IEEE Communications Surveys & Tutorials, vol. 21, no. 3, pp. 2361-2391, thirdquarter 2019, doi: 10.1109/COMST.2019.2915069.

[9] D. W. Matolak and R. Sun, "Air-ground channel characterization for unmanned aircraft systems: The near-urban environment," MILCOM 2015 - 2015 IEEE Military Communications Conference, Tampa, FL, USA, 2015, pp. 1656-1660, doi: 10.1109/MILCOM.2015.7357682.

[10] J. Holis and P. Pechac, "Elevation Dependent Shadowing Model for Mobile Communications via High Altitude Platforms in Built-Up Areas," in IEEE Transactions on Antennas and Propagation, vol. 56, no. 4, pp. 1078-1084, April 2008, doi: 10.1109/TAP.2008.919209.

[11] The MathWorks, Inc. (2023). Communications Toolbox version: 8 (R2023a). Accessed: August 01, 2023. Available: https://www.mathworks.com.

[12] Radiocommunication Sector of International Telecommunication Union. Recommendation ITU-R P.838-3: Specific attenuation model for rain for use in prediction methods. P Series, Radiowave Propagation 2005.

[13] Radiocommunication Sector of International Telecommunication Union. Recommendation ITU-R P.676-10: Attenuation by atmospheric gases 2013.

[14] Crane, Robert K. Electromagnetic Wave Propagation through Rain. Wiley, 1996.

[15] 3GPP TR 22.829 V16.3.0 (2020-06): "Study on enhancement for Unmanned Aerial Vehicles (UAVs)." 3rd Generation Partnership Project (3GPP), Technical Specification Group Services and System Aspects, Release 16.

[16] R. O. Schmidt, "A new approach to geometry of range difference location," IEEE Transactions on Aerospace and Electronic Systems, Vols. AES-8, no. 6, pp. 821-835, 1972.

[17] R. O. Schmidt, "Least Squares Range Difference Location," IEEE Transactions on Aerospace and Electronic Systems, vol. 32, no. 1, pp. 234-242, 1996.

[18] C. Knapp and G. Carter, "The Generalized Correlation Method for Estimation of Time Delay," in proc., *IEEE Trans. Ac., Spch. and Sig. Proc. (ICASSP)*, vol. 44, pp. 320-327, 1976.

[19] L. Zhou, G. Li, Z. Zheng and X. Yang, "TOA Estimation with Cross Correlation-Based Music Algorithm for Wireless Location," in proc., *2014 Fourth International Conference on Communication Systems and Network Technologies*, 2014, pp. 862-865, doi: 10.1109/CSNT.2014.179.

[20] X. Ning, X. Sha and X. Wu, "A TOA Estimation Method for IR-UWB Ranging Systems," in proc., *2010 First International Conference on Pervasive Computing, Signal Processing and Applications*, 2010, pp. 684-687, doi: 10.1109/PCSPA.2010.170.

[21] J. Xu, Z. Wang, Q. Liu and L. Ren, "A novel TOA estimation method for unknown signal based on intra-pulse correlation accumulation," in proc., *2016 IEEE International Conference on Signal Processing, Communications and Computing (ICSPCC)*, 2016, pp. 1-4, doi: 10.1109/ICSPCC.2016.7753696.

[22] W. E. Hoover and U. S., "Algorithms for confidence circles and ellipses," United States National Ocean Service Office of Charting and Geodetic Services, Tech. Rep., 1984, nOAA technical report NOS 107 C&GS 3. [Online] Available: https://repository.library.noaa.gov/view/noaa/23141.

[23] Texas Instruments, "TI LIDAR Pulsed Time of Flight Reference Design," [Online]. Available: https://www.ti.com/lit/pdf/tiducm1b. [Accessed 03 October 2022].

[24] NOAA, "GPS Accuracy," National Coordination Office for Space-Based Positioning, Navigation, and Timing, 3 March 2022. [Online]. Available: https://www.gps.gov/systems/gps/performance/accuracy/. [Accessed 10 August 2022].

[25] S. Knappe, V. Shah, P.D.D. Schwindt, L. Hollberg, J. Kitching, L.-A. Liew and J. Moreland, John, "A microfabricated atomic clock". *Applied Physics Letters*. **85** (9): 1460–1462, Aug. 30, 2004.

[26] J. Kitching, "Chip-scale Atomic Devices," *Applied Physics Letters*, **5**(3):031302, 2018.